Multi-slice helical CT: Scan and reconstruction

Hui Hu[a),b)]
General Electric Company, Applied Science Laboratory, Milwaukee, Wisconsin 53201-0414

(Received 21 April 1998; accepted for publication 27 October 1998)

The multi-slice CT scanner refers to a special CT system equipped with a multiple-row detector array to simultaneously collect data at different slice locations. The multi-slice CT scanner has the capability of rapidly scanning large longitudinal (z) volume with high z-axis resolution. It also presents new challenges and new characteristics. In this paper, we study the scan and reconstruction principles of the multi-slice helical CT in general and the 4-slice helical CT in particular. The multi-slice helical computed tomography consists of the following three key components: the preferred helical pitches for efficient z sampling in data collection and better artifact control; the new helical interpolation algorithms to correct for fast simultaneous patient translation; and the z-filtering reconstruction for providing multiple tradeoffs of the slice thickness, image noise and artifacts to suit for different application requirements. The concept of the preferred helical pitch is discussed with a newly proposed z sampling analysis. New helical reconstruction algorithms and z-filtering reconstruction are developed for multi-slice CT in general. Furthermore, the theoretical models of slice profile and image noise are established for multi-slice helical CT. For 4-slice helical CT in particular, preferred helical pitches are discussed. Special reconstruction algorithms are developed. Slice profiles, image noises, and artifacts of 4-slice helical CT are studied and compared with single slice helical CT. The results show that the slice profile, image artifacts, and noise exhibit performance peaks or valleys at certain helical pitches in the multi-slice CT, whereas in the single-slice CT the image noise remains unchanged and the slice profile and image artifacts steadily deteriorate with helical pitch. The study indicates that the 4-slice helical CT can provide equivalent image quality at 2 to 3 times the volume coverage speed of the single slice helical CT. © *1999 American Association of Physicists in Medicine.* [S0094-2405(99)00401-0]

Key words: multi-slice CT, helical/spiral CT, preferred helical pitch, multi-slice helical interpolation algorithms, z-filtering reconstruction, the volume coverage speed performance, theoretical models

I. INTRODUCTION

Most currently used x-ray CT scanners are the single slice fan-beam CT system. In this system, the x-ray photons emanating from the focal spot of the x-ray tube are first collimated into a thin fan shaped beam [Fig. 1(a)]. After attenuation by the object being imaged, the attenuation profile of this fan-beam, also called the fan-beam projection, is recorded by a single row of detector array, consisting of roughly a thousand detector elements.

There are two modes for a CT scan: step-and-shoot CT or helical (or spiral) CT. For step-and-shoot CT, it consists of two alternate stages: data acquisition and patient positioning. During the data acquisition stage, the patient remains stationary and the x-ray tube rotates about the patient to acquire a complete set of projections at a prescribed scanning location. During the patient positioning stage, no data are acquired and the patient is transported to the next prescribed scanning location. The data acquisition stage typically takes one second or less while the patient positioning stage is around one second. Thus, the duty cycle of the step-and-shoot CT is 50% at best. This poor scanning efficiency directly limits the volume coverage speed versus performance and therefore the scan throughput of the step-and-shoot CT.

The term volume coverage speed versus performance (or the volume coverage speed performance for short) refers to the capability of rapidly scanning a large longitudinal (z) volume with high longitudinal (z-axis) resolution and low image artifacts. The volume coverage speed performance is a deciding factor for the success of many medical CT applications which require a large volume scanning (e.g., an entire liver or lung) with high image quality (i.e., high z-axis resolution and low image artifacts) and short time duration. The time duration is usually a fraction of a minute and is imposed by (1) short scan duration for improved contrast enhancement and for reduced usage of the contrast material; (2) patient breathhold period for reduced respiratory motion; and/or (3) maximum scan duration without experiencing a lengthy tube cooling delay. Thus, one of the main themes in CT development is to improve its volume coverage speed performance.

Helical (or spiral) CT[1–4] was introduced around 1990. In this mode, the data are continuously acquired while the patient is simultaneously transported at a constant speed through the gantry. The patient translating distance per gantry rotation in helical scan is referred to as the table speed. Because the data are continuously collected without pausing, the duty cycle of the helical scan is improved to nearly 100%

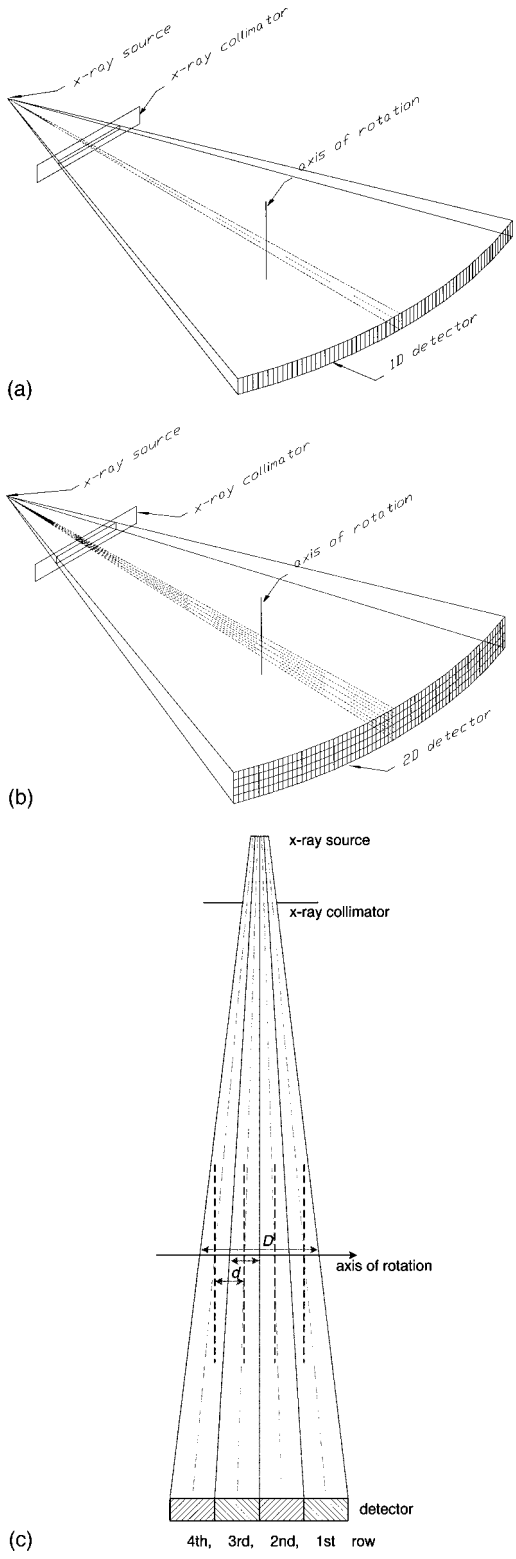

FIG. 1. (a) Perspective view of the single slice CT scanner. (b) Perspective view of the multi-slice CT scanner. (c) Cross-section view of the multi-slice CT scanner and parallel fan-beams vs cone beam imaging geometries.

and the volume coverage speed performance can be substantially improved.

To realize this improvement, several helical reconstruction algorithms have been developed.[2–6] These algorithms, with variable degrees of success, help to reduce the adverse slice profile broadening and the artifacts induced by the simultaneous table translation. Two commonly used helical reconstruction algorithms are the 360° and 180° linear interpolation (LI). The 360° LI algorithm[2–4] explores the 360° periodicity in the projection data due to the fact that the projection data 360° apart would be identical in the absence of patient motion, noise variation and other errors. It uses two sets of helical CT projections 360° apart to estimate one set of projections at a prescribed location. On the other hand, the 180° LI algorithm[3,5] (also called the half-scan with interpolation or extrapolation algorithm), utilizes the 180° periodicity in the projection data due to the fact that the two measurements along the same path but in the opposite directions (180° apart) would be the same in the absence of patient motion, noise variation and other errors. It uses two sets of helical CT projections 180° apart to estimate one set of projections at a prescribed location.

Helical CT has become the method of choice for many routine and new clinical applications. It provides good image quality for body imaging applications at a table advancement per rotation of 1 to 2 times the x-ray beam collimation. However, the table advancement per rotation of twice the x-ray beam collimation appears to be the limit of the volume coverage speed performance of a single slice CT, and further increase of the table translation would result in clinically unusable images.[7,8] On the other hand, many time-critical and/or *z*-axis resolution-critical applications, such as multiphase organ dynamic studies and CT angiography studies using 3D, multi-planar reformation (MPR) or maximum intensity projection (MIP) techniques, would be benefited by improved volume coverage speed performance. To be specific, a better volume coverage speed performance would enable users to further increase the *z*-axis resolution and/or coverage of a CT exam, to further reduce the amount of contrast material used, and to better separate the arterial and venous phases in data acquisitions.

The so-called multi-slice CT scanner seems to be a next step for a substantial improvement of the volume coverage speed performance. The multi-slice CT scanner refers to the special CT system equipped with a multiple-row detector array [Figs. 1(b) and 1(c)], as opposed to a single-row detector array. It allows for simultaneous scan of multiple slices at different *z* locations. We refer to the multi-slice CT scanner with *N* detector rows as the *N*-slice CT scanner, containing roughly *N* thousand individual detector elements. Previously, a 2-slice CT scanner (Twin by Elscint Inc.)[9] was introduced and its physical performance has been investigated by Liang and Kruger.[10] The scanner discussed in this paper is a 4-slice scanner (LightSpeed QX/i by General Electric Company).

Due to the distinct differences in scanner construction, the multi-slice CT scanner exhibits complex imaging characteristics and calls for new scan and reconstruction strategies. In this paper, we present new theoretical developments of multi-slice helical CT in general and 4-slice helical CT in particular, which serve as the foundation for the system and operation design of the 4-slice CT scanner discussed. In Sec. II, we first discuss some new concepts in multi-slice CT to

set the stage for discussion. In Sec. III, we investigate an important characteristic in multi-slice helical CT data acquisition—preferred helical pitch. In Sec. IV, we present the helical reconstruction algorithms for the multi-slice CT. In Sec. V, we establish the theoretical models of noise and slice profile of the multi-slice CT and assess the performance of the 4-slice CT scanner using these models and computer simulations.

II. NEW CONCEPTS IN MULTI-SLICE CT

Compared with its single slice counterpart, the multi-slice CT is intrinsically more complex and introduces several new concepts. We discuss two new concepts in this section.

A. Detector row collimation versus x-ray collimation

In the single slice CT [see Fig. 1(a)], the x-ray beam collimation (or, the thickness of the x-ray beam) affects both the *z* volume coverage speed and the *z*-axis resolution (the slice thickness). A thick x-ray collimation is preferred for large volume coverage speed while a thin collimation is desirable for high *z*-axis resolution. The single slice CT users are confronted with the conflicting requirements when both large volume coverage speed and high *z*-axis resolution are needed. In the single slice CT, the detector row collimation is either not used or used as a part of the x-ray beam collimation (i.e., the post-patient collimation).

One of the enabling components in multi-slice CT system is the multi-row detector array. The use of multiple detector rows enables us to further divide the total x-ray beam (still prescribed by the x-ray beam collimation) into multiple subdivided beams (prescribed by the detector row collimation also called the detector row aperture), referring to Figs. 1(b) and 1(c). In the multi-slice CT system, while the total x-ray collimation still indicates the volume coverage speed, the detector row collimation, rather than the total x-ray collimation, determines the *z*-axis resolution (i.e., the slice thickness).

With reference to Figs. 1(b) and 1(c), we use D and d to denote the x-ray beam collimation and the detector row collimation, respectively. Consistent with the convention, both D and d are measured at the axis of rotation. If the gaps (i.e., the dead area) between adjacent detector rows are small and can be ignored, the detector row spacing equals to the detector row collimation, also denoted as d. The detector row collimation (or spacing), d, and the x-ray beam collimation, D, has the following relationship:

$$d(mm) = \frac{D(mm)}{N}, \tag{1}$$

where N is the number of detector rows.

In single slice CT, the detector row collimation equals to the x-ray beam collimation and these two parameters can be used interchangeably. In the multi-slice CT, the detector row collimation is only $1/N$ of the x-ray beam collimation. This much improved (relaxed) relationship makes it possible to simultaneously achieve high volume coverage speed and high *z*-axis resolution. In general, the larger the number of detector rows N, the better the volume coverage speed performance.

B. Cone-beam geometry versus parallel fan-beams geometry

The x-ray photons emanating from the focal spot of the x-ray tube describe a divergent beam. We use the ray bundle to capture the effect of the area integration due to the finite size (i.e., aperture) of detector cells. The effective trace of each ray bundle is described by the center line of the ray bundle, as shown in Figs. 1(a), 1(b), and 1(c) by the light dashed lines.

In the single slice CT, the ray bundles lie in the gantry plane—the plane normal to the axis of gantry rotation. However, they fan out within the gantry plane and this divergence is correctly accounted for by the fan-beam imaging geometry, which calls for the fan-beam reconstruction algorithm.

In the multi-slice CT [referring to Figs. 1(b) and 1(c)], the ray bundles not only fan out within the gantry plane but also diverge from the gantry plane. This imaging geometry is called the cone-beam imaging geometry, which calls for special cone-beam reconstruction algorithms. Many cone-beam reconstruction algorithms have been developed for both step-and-shoot CT[11,12] and helical CT.[13–15] All of them require fundamentally different data processing schemes from that of the existing fan-beam reconstruction.

Because the scanner discussed has a relatively small number of detector rows ($N=4$) and therefore relatively small cone-beam divergent effect, we use the multiple, parallel fan-beams, as illustrated in Fig. 1(c), to approximate the cone-beam geometry. To be specific, the projection measurements by each detector row are treated as if they were acquired with a fan-beam within the gantry plane at the axial location where the subdivided x-ray beam intercepts the axis of rotation, referring to the dark dashed line in Fig. 1(c). This approximation allows the use of the existing fan-beam based computing system.

III. MULTI-SLICE HELICAL CT DATA ACQUISITION: PREFERRED HELICAL PITCHES

Data acquisition and image reconstruction are the two aspects of CT that affect the quality of the reconstructed images. The multi-slice helical CT data acquisition is discussed in this section and the image reconstruction is in the next section.

A. Extended definition of the helical pitch

The pitch of a helical scan refers to the ratio of the table translating distance per gantry rotation to the thickness of the individual x-ray beam. Let p and s be the helical pitch and table translating distance per gantry rotation, respectively. In the single slice CT, the x-ray beam thickness is determined by the beam collimation setting. The helical pitch for single slice CT is defined as

$$p=\frac{s(mm)}{D(mm)}. \tag{2a}$$

On the other hand, in the multi-slice CT, the thickness of the individual x-ray beam is determined by the detector row collimation, as opposed to the x-ray beam collimation. Thus, the definition of the helical pitch for the multi-slice CT can be extended as

$$p=\frac{s(mm)}{d(mm)}. \tag{2b}$$

For example, a 4-slice CT scan using 5 mm row collimation (and therefore 20 mm x-ray beam collimation) and at 15 mm table translating distance per rotation will result in a helical pitch of $3(=15/5)$ rather than $0.75(=15/20)$.

It is noted that with reference to Eq. (1), the definition of the helical pitch for the multi-slice CT [Eq. 2(b)] reduces to that for the single slice CT [Eq. 2(a)] when the single slice CT is considered. It is also noted that consistent with the single slice CT definition, the helical pitch of the multi-slice CT still indicates roughly the number of contiguous slices that can be generated over the table translating distance in one gantry rotation.

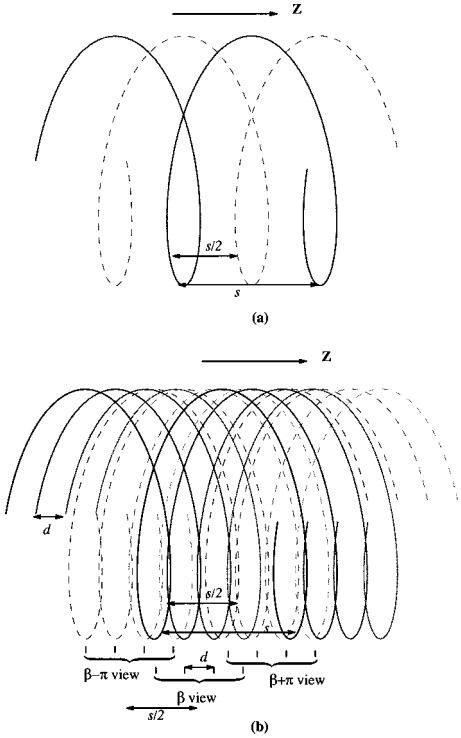

FIG. 2. Illustration of the z sampling pattern (the helices pattern) resulting from the (a) single slice helical CT and (b) multi-slice helical CT.

B. Preferred helical pitch

One characteristic in the multi-slice helical CT data acquisition is the existence of the preferred helical pitch. Due to the use of multi-row detector array, projection data along a given path may be measured multiple times by different detector rows. One important consideration in multi-slice helical CT data acquisition is to select a preferred helical pitch to reduce the redundant measurements and therefore to improve the overall data z sampling efficiency. In this section, we first review the single slice helical CT and propose a new z sampling analysis method. We then investigate the concept of preferred helical pitch in the multi-slice helical CT data acquisition using the z sampling analysis.

In the single slice helical scan, the x-ray beam describes a spiral path (i.e., a helix) around the patient, as shown by the solid line in Fig. 2(a). Each point on the helix represents a set of fan-beam projection measurements, where the gantry rotation angle and the z location of the fan-beam are denoted by the rotation angle and the z position of the helix. Furthermore, as mentioned in the Introduction, the projection data exhibit the 180° periodicity that the two measurements along the same path in the opposite directions would be identical in the absence of patient motion, noise variation, and other errors. By exploring this 180° periodicity, actual fan-beam measurements can be regrouped to generate a set of complementary fan-beam projections, which is illustrated by the dashed helix in Fig. 2(a).

Similarly, in the multi-slice helical CT, the multiple subdivided x-ray beams defined by multiple (N) detector rows describe multiple (N) interlacing helices. The helices representing different detector rows are shown by the differently shaded solid lines in Fig. 2(b). Furthermore, utilizing the 180° periodicity results in additional complementary fan-beam projections, which are illustrated by the multiple, differently-shaded, dashed helices in Fig. 2(b). These interlacing helices form one set of multi-slice helical CT data.

The z gap of the helix pattern represents the z sampling spacing of the projection data to be used in the interpolation. Thus, the z gap of the helix pattern determines the effectiveness of the interpolation and therefore is a good indicator of the image quality (IQ) (in terms of the slice profile and image artifacts). The smaller the z gap, the better the IQ of the helical CT. We propose to use the z gap to characterize the IQ of helical CT and call this method the z sampling analysis.

The z gap information can be derived from the z sampling positions. We use β_0 to denote the gantry rotation angle when the table is at location z_0. Thus, the z sampling positions of the measurements acquired at the gantry rotation angle β is given by the following equation:

$$z=z_0+\frac{s}{2\pi}(\beta-\beta_0)-Z_n d, \tag{3a}$$

where

$$Z_n=\left(-\frac{N+1}{2}+n\right). \tag{3b}$$

In Eq. 3(a), the second term describes the table translation in helical CT as the gantry rotates. The third term depicts the z displacements from the gantry plane due to the use of different detector rows. For example, $Z_n=0$ for the single slice CT; $Z_n=[-1.5,-0.5,0.5,1.5]$ for the 4-slice CT [referring to Fig. 1(c)]. n is the detector row index, ranging from 1 to N.

For the single slice helical CT and with reference to Eqs. 2(b), (3), and Fig. 2(a), the z gap of 360° LI [i.e., the gap of the solid helix in Fig. 2(a)] is equal to s or pd while the z gap of 180° LI (the gap between the solid and dashed helices) is equal to $s/2$ or $(p/2)d$. This explains why 180° LI yields a better IQ than 360° LI. Furthermore, varying the table speed will stretch or compress the helices (both solid and dashed) together but will not change this uniform helix pattern. As helical pitch increases, the z gap of the helix pattern steadily increases and therefore the IQ steadily deteriorates.

For the multi-slice helical CT and with reference to Eqs. (2b), (3), and Fig. 2(b), the projection z sampling positions at a given gantry rotation angle β can be derived from the solid helices and are indicated by a group of the vertical bars denoted as the β view. Similarly, the z sampling positions of the complementary views that are $\pm 180°$ from the β view can be derived from the dashed helices and are represented by the two groups of vertical bars denoted as the $\beta \pm \pi$ views, respectively. The relative displacement of all the samples of these views determines the z gap, and therefore the helix pattern. It is noted from Eq. (3) and Fig. 2(b) that while the z displacement between a view and its complementary views (i.e., between the solid and dashed helices of the same detector row) is still $s/2$, or $(p/2)d$, the displacement of the z positions between the adjacent detector rows within a view equals to the detector row spacing, d. Thus, the z gap is determined by the two scan parameters; helical pitch p and detector row spacing d. As the helical pitch varies, distinctively different z sampling patterns and therefore interlacing helix patterns may result in the multi-slice helical CT.

To illustrate the distinct change in z sampling pattern as the helical pitch varies, a 4-slice scanner operating at 2:1 and 3:1 helical pitches, respectively, is considered. In this discussion it is assumed that the 180° periodicity is utilized. For the 2:1 helical pitch $(p=2)$, as shown in Fig. 3(a), the displacement of the z sampling positions between the solid and dashed helices is d $(=(p/2)d)$, which is the same as the displacement from one solid helix to the next. This causes a high degree of overlap between different helices, generating highly redundant projection measurements at certain z positions. Because of this high degree of redundancy (or, inefficiency) in z sampling, the overall z sampling spacing (i.e., the z gap of the interlacing helix pattern) is still d, not any better than its single slice counterpart. On the other hand, for the 3:1 helical pitch $(p=3)$, the displacement of the z sampling positions between the solid and dashed helices is 1.5 d $(=(p/2)d)$. This special shift allows the dashed helices bisecting the gap of the solid ones, reducing the overall z gap (the z sampling spacing) to $d/2$, as shown in Fig. 3(b). It is noted that even though the volume coverage speed of the 3:1 pitch is 50% faster than the 2:1 pitch, the z gap (the z sampling spacing) in the 3:1 pitch is only one-half of that in the 2:1 pitch and therefore the IQ of the 3:1 pitch helical CT is better than that of the 2:1 pitch.

In general, one of the new challenges in multi-slice helical CT is to use a multi-row detector array efficiently, i.e., to achieve efficient z sampling. As illustrated by the above example, only at certain helical pitches, the measurements from different detector rows are relatively unique and complementary to each other. Only at these helical pitches, the volume coverage speed performance of the multi-slice scanner is substantially better than its single slice counterpart. Thus, the selection of helical pitches becomes even more critical to the performance of the multi-slice CT than the single slice CT. The pitch selection in the multi-slice CT is determined by the consideration of the z-sampling efficiency as well as by other conventional factors, such as the volume coverage speed (which disfavors very low helical pitch), slice profile and image artifacts (which disfavor very high helical pitch). The pitches selected to represent the preferred tradeoffs for various applications are called the preferred helical pitches. The preferred helical pitches for the 4-slice scanner will be discussed in Sec. V C.

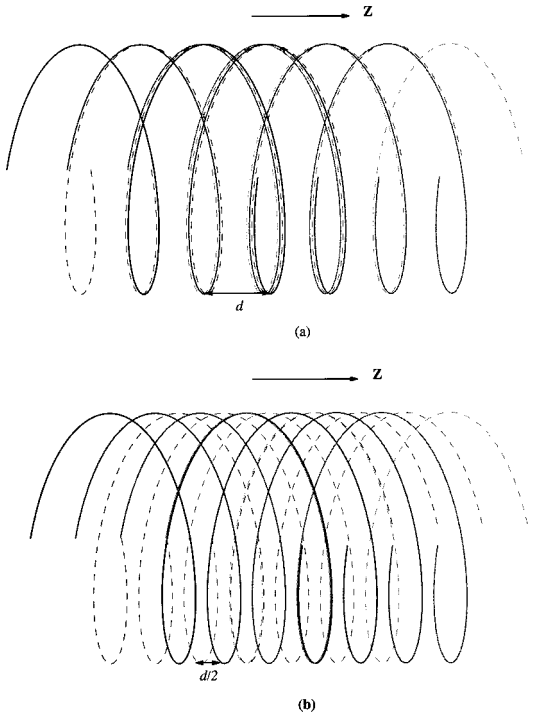

FIG. 3. Special z sampling pattern (the helices pattern) of the 4-slice helical CT at pitch (a) 2:1 and (b) 3:1.

IV. MULTI-SLICE HELICAL RECONSTRUCTION ALGORITHMS

Besides the data acquisition efficiency discussed in the previous section, CT image quality is also determined by the accuracy of reconstruction algorithms. In this section, we present the reconstruction strategy and linear interpolation algorithms[16] for multi-slice helical CT in general. Two reconstruction algorithms[16,17] are included in Appendix A for the 4-slice helical CT in particular. We also introduce the concept of the z-filtering reconstruction.[16,18,19]

A. Linear-interpolation reconstruction algorithms

The multi-slice helical scan generates multiple sets of measurements at each rotation angle. The z locations of these measurements are indicated by the interlacing helices in Fig.

2(b). Similar to its single slice counterpart, the multi-slice helical reconstruction consists conceptually of the following two steps: (1) from these interlacing helical data, estimate a set of complete projection measurements at a prescribed slice location; (2) reconstruct the slice from the estimated projection set using the step-and-shoot reconstruction algorithm.

In general, the estimation of the projection data along a given projection path is obtained by weighted averaging (interpolating) the contributions of those measurements from all detector rows that would be along the same projection path if the differences in z sampling positions due to the table translation and the displacement of multiple detector rows were ignored. The contribution (the weighting factor) of a measurement is determined by how close the z location of the measurement to the slice location. The closer it is, the larger contribution a measurement represents. Reconstructing an image normally requires the projection measurements from all detector rows.

In the case of two-point linear interpolation, the two measurements closest to the slice location along the z direction are used in the interpolation. Preferably, the two measurements should be on opposite sides of the reconstructed slice. To mathematically describe this general linear interpolation algorithm, we introduce a few nomenclatures. We denote multi-slice fan-beam projection measurements as $P_n(\beta,\gamma)$, where β denotes the gantry rotation angle of a given view; γ the fan angle of a given detector channel in the given view; and n the detector row index (ranging from 1 to N). We use z_0 to denote the z location of the slice to be reconstructed and $P_{n_1}(\beta_1,\gamma_1)$ and $P_{n_2}(\beta_2,\gamma_2)$ to denote the two actual measurements used in a linear interpolation to estimate a projection measurement $P(\beta,\gamma)$ at z_0. The z locations of these two measurements can be derived from Eq. (3) and are denoted as z_1 and z_2. Thus, the two-point linear interpolation algorithm can be described by the following equation:[16]

$$P(\beta,\gamma)=w_1P_{n_1}(\beta_1,\gamma_1)+w_2P_{n_2}(\beta_2,\gamma_2),$$

where

$$w_1=\frac{z_2-z_0}{z_2-z_1};\quad w_2=1-w_1=\frac{z_0-z_1}{z_2-z_1}. \tag{4}$$

The interpolation described in Eq. (4) is general and applicable to CT systems of any number of detector rows and any helical pitch. However, it does not provide the information as to which portion of the data from a given detector row contributes to the slice reconstruction at the given location. This information is important for efficient implementation. Furthermore it does not address how to handle the redundant data measurements when they occur.

Special helical interpolation algorithms that are suitable for efficient implementation and that correctly handle redundant measurements may be derived for a given number of detector rows (N) and for a certain range of helical pitches (p). Two special linear interpolation reconstruction algorithms for the 4-slice helical CT are given in Appendix A for helical pitches around 3 (between 2.6 and 3.2)[16] and around 6 (between 5.3 and 8).[17] In general, we use $W_n(\beta,\gamma)$ to denote the helical interpolation weighting function—the amount of contribution—for projection measurements $P_n(\beta,\gamma)$. As an example, for helical pitch around 3, the portion of projection measurements which has nonzero contribution to a reconstructed slice is derived from Eq. (A4) and is shown by the shaded regions in Fig. 4. This information is used for efficient implementation.

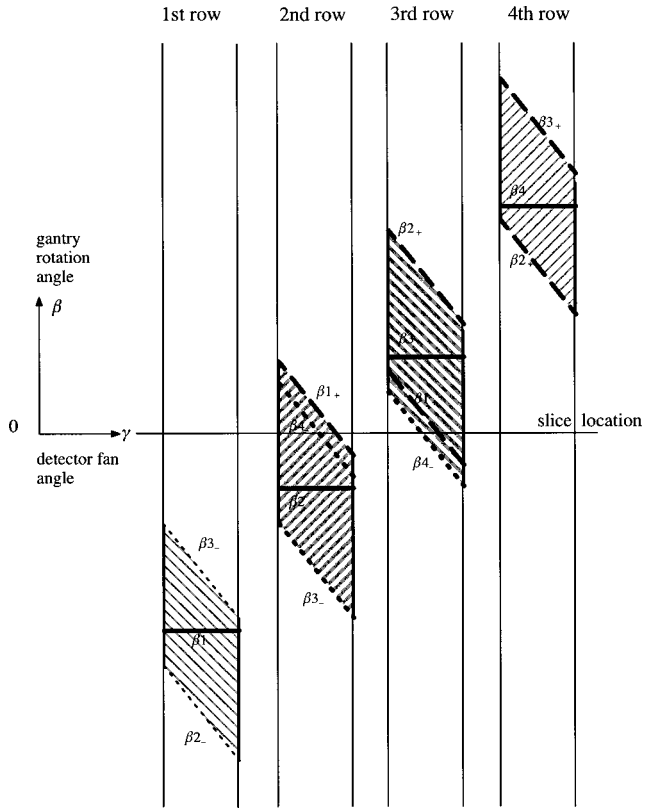

FIG. 4. Illustration of z sampling pattern and data utilization for a 4-slice helical CT at pitch around 3:1.

It is noted that the algorithms proposed here are interpolative, the weighting function derived is exclusively in the range [0,1], and is continuous everywhere.

B. *Z*-filtering (variable-thickness) reconstruction

Similar to what has been noted for the single slice helical CT,[18,20] the two-point linear interpolation algorithm of the multi-slice helical CT can only provide fixed slice thickness and therefore a fixed tradeoff of slice thickness versus image noise and artifacts given the scanning parameters. It is desirable to provide different tradeoffs tailored to different application requirements. Reconstructing images with multiple slice thickness calls for a new type of helical reconstruction algorithm, referred to as the z-filtering (or variable-thickness) reconstruction algorithm,[19] which contains z-filtering (or z-axis resolution) parameters in reconstruction to further control the tradeoff of the slice thickness versus image noise and artifacts.

One approach to extend the two-point linear interpolation algorithms to the z-filtering reconstruction algorithms can generally be described as forming a composite slice by com-

bining several slices reconstructed with the two-point linear interpolation reconstruction algorithm. In implementation, the composite slice can be reconstructed directly without generating the original slices. This approach was originally developed for multi-slice CT[19] [refer to Eq. (B3) in Appendix B] and has been first applied to single slice CT.[8,20] Alternatively, the *z*-filtering concept can directly be integrated into the helical interpolation algorithm, as shown in Appendix B [Eq. (B4)].[16] The *z*-filtering reconstruction algorithm allows for interpolation of more than two points.

With the *z*-filtering reconstruction algorithm, slice profile, image noise, and image artifacts are controlled not only by the scan parameters (such as helical pitch, beam collimation, and mA), but also by the *z*-filtering parameters in reconstruction. Thus, the tradeoff of the slice thickness versus image noise and artifacts are no longer fixed for given scanning parameters. They are also controlled by reconstruction parameters. The *z*-filtering reconstruction enables users to generate from a single CT scan multiple image sets, representing different tradeoffs of the slice thickness, image noise and artifacts to suit for different application requirements.

V. PERFORMANCE OF MULTI-SLICE HELICAL CT

Similar to what has been noted for single slice CT,[3,21,5,7] for multi-slice CT, the image quality of the helical CT differs from the step-and-shoot CT in terms of the slice profile, image noise, and artifacts. The theoretical models of the slice profile and image noise of the multi-slice helical CT are developed in Sec. V A. From these theoretical models and computation simulations, slice profile, image noises, and artifacts of the 4-slice helical CT are studied and compared with single slice helical CT for various helical pitches in Sec. V B. The results are discussed and the volume coverage speed performance of the 4-slice helical CT is also assessed in Sec. V C.

A. Slice profile and noise of multi-slice helical CT: Theoretical models

In this section, we first briefly review the theoretical model of the slice profile for single-slice CT. We also provide a new intuitive noise model for single-slice CT. We then extend the theoretical models of slice profile and noise to multi-slice CT. For simplicity, we only consider the slice profile and image noise measured around the axis of rotation.

The slice profile and image noise of single slice CT have been modeled theoretically.[5,6,21–24] We denote the helical interpolation weighting function at the center detector channel ($\gamma=0$) as $w(\beta)$ or $w(z)$. The slice profile, denoted as $sp(s,d,z_s)$, can be expressed as the following convolution:[24]

$$sp(s,d,z_s)=\int dz b(z) w(z-z_s), \tag{5a}$$

where $b(z)$ is the slice profile of step-and-shoot CT at the same collimation d and the z_s is the distance along z axis to the reconstructed slice.

In this paragraph, we present a new intuitive noise model for the single slice CT, which is derived based on the works of Refs. 21 and 6. We use σ_0 to denote the noise standard deviation in the projection data after reconstruction kernel (the in-plane filter) is applied. By applying the helical weighting factor, $w(\beta)$, the noise standard deviation of the weighted projection becomes $w(\beta)\sigma_0$. We further use σ to denote the noise measured at the central region of the reconstructed image. It follows from the noise propagation analysis that

$$\sigma^2=\int d\beta w^2(\beta)\sigma_0^2, \tag{6}$$

where the integration is over those β where $w(\beta)$ is nonzero. Furthermore, we denote the image noise of helical and step-and-shoot (axial) CT as σ_H and σ_A, respectively. For the full rotation step-and-shoot scan, one has $w(\beta)=\frac{1}{2}$ for $0\leqslant\beta\leqslant 2\pi$ and therefore from Eq. (6) the image noise is $\sigma_A^2=(\pi/2)\sigma_0^2$. With other parameters being equal, the noise ratio of helical to step-and-shoot CT can be expressed as follows:

$$\frac{\sigma_H}{\sigma_A}=\sqrt{\frac{2}{\pi}\int d\beta w^2(\beta)}. \tag{7a}$$

It can be proven that this noise model is in good agreement with the theoretical and experimental results published in the literatures.[3,21,22]

The theoretical models of the slice profile and noise for the multi-slice CT are established with similar mathematical analyses. Noting that in the multi-slice CT the data may come from different detector rows, Eqs. (5a) and (7a) can be extended for multi-slice CT as follows:

$$sp(s,d,z_s)=\int dz b(z)\sum_{n=1}^{N} w_n(z-z_s), \tag{5b}$$

$$\frac{\sigma_H}{\sigma_A}=\sqrt{\frac{2}{\pi}\int d\beta\sum_{n=1}^{N} w_n^2(\beta)}, \tag{7b}$$

where, $w_n(\beta)$ or $w_n(z)$ stands for the helical interpolation weighting factor at the center detector channel ($\gamma=0$) of the nth detector row. The general slice profile and noise models of multi-slice CT [Eqs. 5(b) and 7(b)] reduce to the result of Liang and Kruger[10] when the 2-slice CT system is considered.

B. IQ evaluations of the 4-slice helical CT

In this section, we study the IQ (i.e., slice profile, image noise, and artifacts) of the 4-slice helical CT for various helical pitches. Since different reconstruction algorithms may result in different slice profiles and image noises, we study the thinnest slice profile achievable from the linear interpolation reconstruction and the lowest image noise achievable at the thinnest slice profile. To be specific, the special reconstruction algorithms described in Eqs. (A4) and (A5) were used to study the IQ performance of the 4-slice CT at helical pitches of 3 and 6, respectively. The general algorithm described in Eq. 4 was used to study IQ performance of the 4-slice CT at other helical pitches.

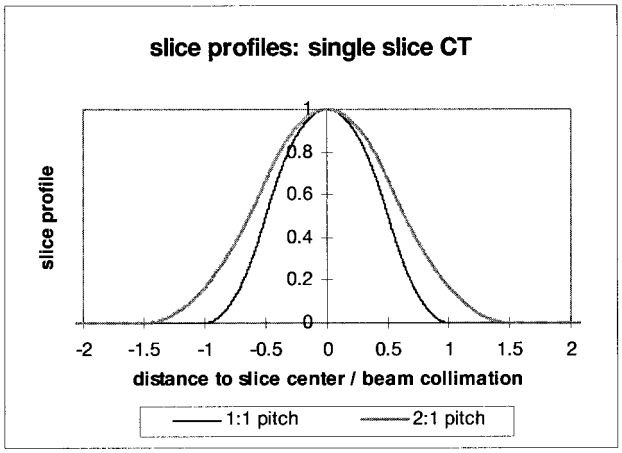

(a)

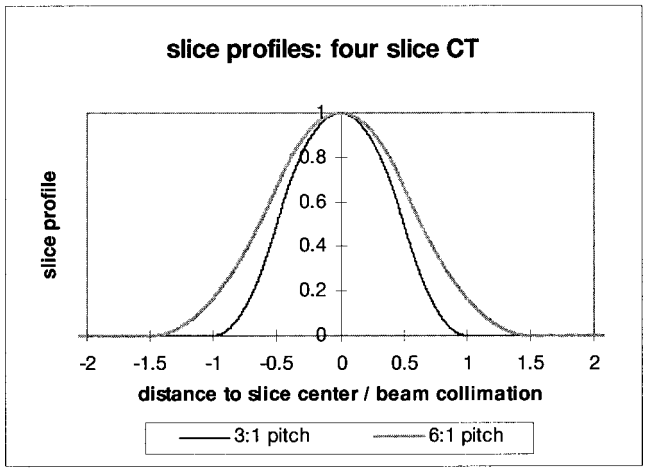

(b)

FIG. 5. Slice profiles of (a) the single slice CT with helical pitches 1 and 2 and (b) the 4-slice CT with helical pitches 3 and 6.

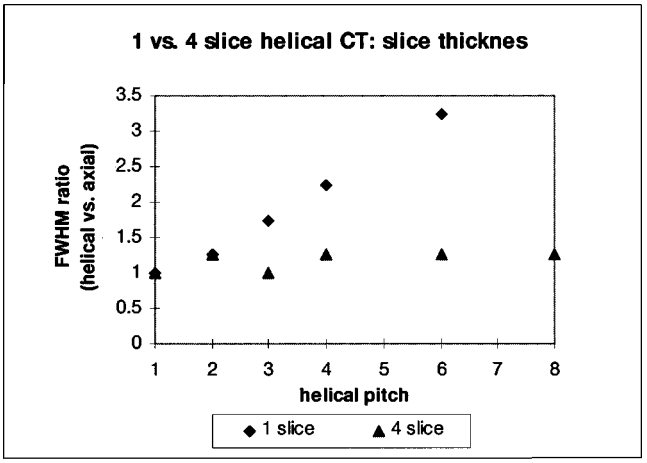

(a)

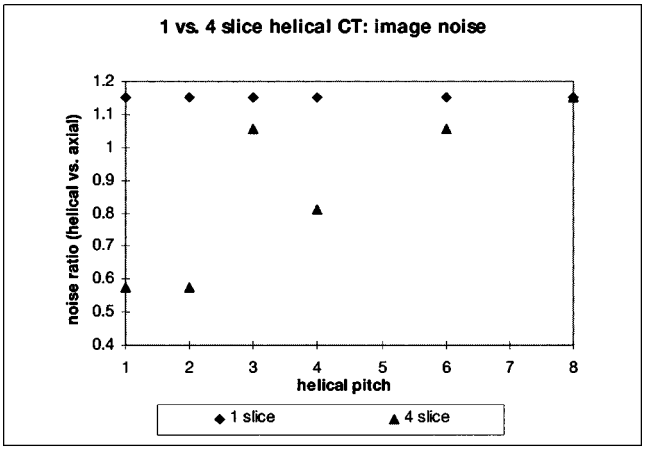

(b)

FIG. 6. Plots of the ratios (helical vs axial) of (a) the slice thickness and (b) the noise of the 4-slice CT versus single slice CT for various helical pitches.

The slice profiles were derived using Eqs. (5a) and (5b) for the single slice and 4-slice helical CT, respectively. Four profiles displayed are the single slice CT with helical pitches 1 and 2 [Fig. 5(a)] and the 4-slice CT with helical pitches 3 and 6 [Fig. 5(b)], respectively. From these slice profiles, the ratios of helical versus step-and-shoot CT in terms of full width at half-maximum (FWHM) and full width at tenth-maximum (FWTM) are tabulated in Table I and FWHM ratios are plotted in Fig. 6(a) for various helical pitches. For each case, the noise ratios of helical versus step-and-shoot CT were computed using Eqs. (7a) and (7b) for single slice and 4-slice helical CT, respectively, and the results are in Table I and shown in Fig. 6(b).

TABLE I. Slice profile and noise comparisons (1 vs 4 slice CT).

	Single slice CT			4-slice CT		
Helical pitch	FWHM ratio	FWTM ratio	Noise ratio	FWHM ratio	FWTM ratio	Noise ratio
0	1.00	1.00	1.00	1.00	1.00	1.00
1	1.00	1.56	1.15	1.00	1.56	0.57
2	1.27	2.23	1.15	1.27	2.23	0.57
3	1.75	3.00	1.15	1.00	1.56	1.05
4	2.25	3.82	1.15	1.27	2.23	0.81
6	3.25	5.52	1.15	1.27	2.23	1.05
8	4.25	7.27	1.15	1.27	2.23	1.15

Computer simulations were conducted to study the image artifacts of both 4-slice and single slice CT systems at various helical pitches. The distances from the x-ray focal spot to the detector and to the axis of rotation were 94.9 cm and 54.1 cm, respectively. The noises were added to simulate the data acquisition with a constant mA. With reference to Fig. 7, the mathematical phantom used in this study consists of a long elliptical cylinder (0 HU) simulating the human body, a set of tilted rods (600 HU) at the edge of the elliptical cylinder simulating the ribs, a disk (400 HU) simulating the spin disk and an air cavity (−1000 HU) simulating the bowel structure. Figure 7 shows the reconstructed images at the same slice location from two CT systems and with various scan and reconstruction parameters. The images displayed represent a region of $40\times26\,\mathrm{cm}^2$. The display window is [width, 150 HU; level, 0 HU]. The table speed and the FWHM are listed on the top of each image.

The images in the top two rows in Fig. 7 were from the single slice CT system with the x-ray collimation of 2.5 mm

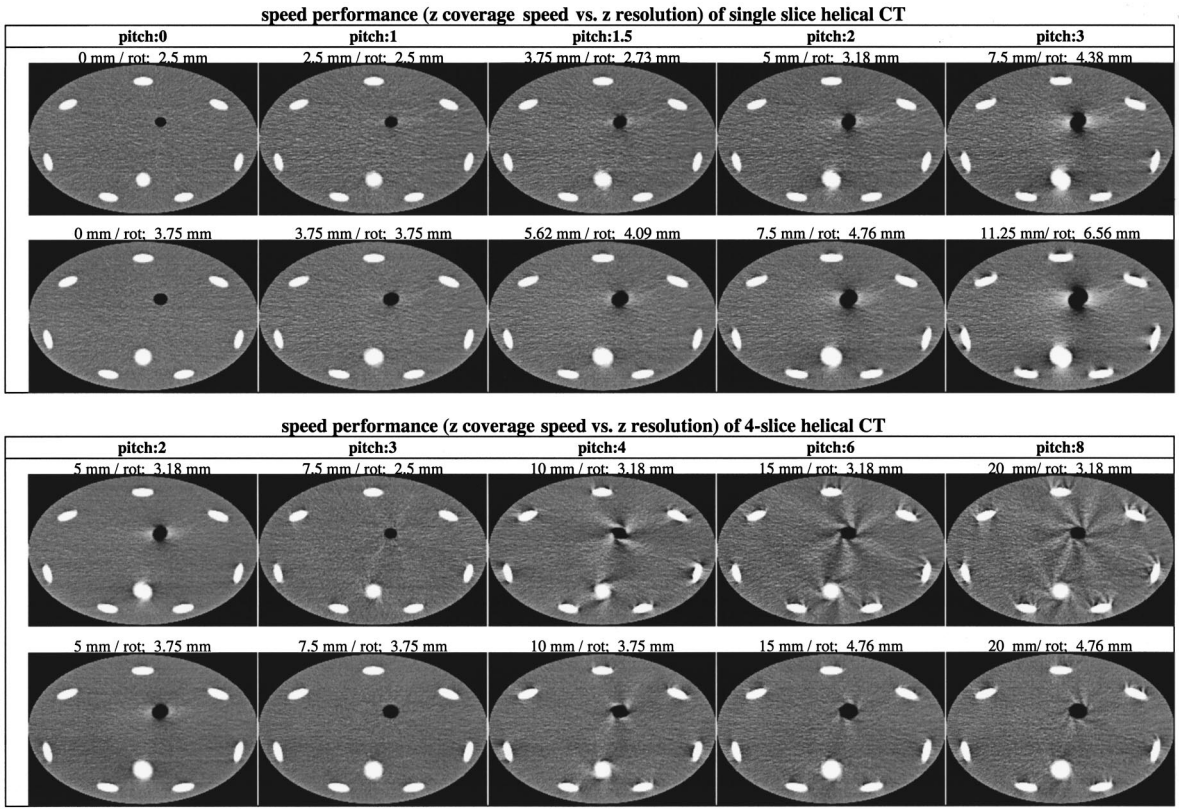

FIG. 7. Computer simulations for comparison of image artifacts at various helical pitches of 4-slice and single slice CT systems.

and 3.75 mm, respectively. With these two collimations, the helical pitches of 0 (the step-and-shoot CT), 1, 1.5, 2, and 3 were simulated and the resulted images are displayed from left to right.

The images of the bottom two rows were from the 4-slice CT system with the 2.5 mm detector row collimation and helical pitches of 2, 3, 4, 6, and 8, respectively (displayed from left to right). Each column of the bottom two rows were reconstructed from the same data set. The top image represents the thinnest slice thickness achievable from the linear interpolation reconstruction. The bottom image, obtained by selecting appropriate z-filter in reconstruction, has a FWHM of 3.75 mm for pitches 2–4 and 4.76 mm for higher pitches.

C. Discussions

1. Existence of the preferred helical pitch

The existence of the preferred helical pitch in a multi-slice helical CT, as discussed in Sec. III B, is clearly demonstrated by the images in Fig. 7 and the data in Table I. The IQ (in terms of the slice profile and image artifacts) of the 3:1 helical pitch (the 2nd column) is substantially better than that of the 2:1 helical pitch (the 1st column) even though the z coverage speed of the 3:1 pitch is 50% higher. These results also validate the z sampling analysis method proposed in Sec. III B.

The results shown in Table I and Figs. 6 and 7 indicate one important difference between the multi-slice and single slice helical CT. In the multi-slice helical CT, the slice profile, image artifacts and noise exhibit the resonance behavior, i.e., have performance peaks or valleys at certain helical pitches, whereas in the single-slice helical CT the slice profile and image artifacts steadily deteriorate and the image noise remains unchanged as helical pitch increases.

2. Preferred helical pitches of the 4-slice CT scanner

The 4-slice CT scanner currently discussed allows a scan taken at two helical pitches, namely, 3:1 and 6:1 pitches. The preferred helical pitches selected represent our attempt to balance the volume coverage speed (determined by the helical pitch) and various aspects of IQ (determined by the z sampling efficiency, helical pitch, and other factors). Providing selected helical pitches also simplifies the user interface.

The 3:1 helical pitch is provided for those applications demanding good contrast resolution and low image artifacts, which are currently done with 1–1.5 pitch single slice helical CT. In fact, with reference to Sec. III B and particularly Figs. 3(b) and 2(a), it is proven using the z sampling analysis that the 3:1 pitch 4-slice helical CT matches the z sampling gap of the 1:1 pitch single slice helical CT, which is $d/2(=(p/2)d)$ with 180° LI. As is further discussed in Sec. V C 4, the 3:1 pitch is the highest helical pitch in the 4-slice CT that can match the z sampling gap of the 1:1 pitch single slice helical CT.

In addition, 3:1 helical pitch provides better control of the cone-beam artifacts. With reference to Fig. 1(c) the x rays

detected by the 1st and 4th detector rows experience more cone-beam effect than the inner two detector rows, and they are tilted in the opposite directions. At 3:1 helical pitch and with reference to Fig. 3(b), the measurements derived from the 1st and 4th detector rows overlap in z sampling locations and therefore can be averaged. Thus, the cone beam effects of the opposite tilted x rays can be partially canceled. It is noted that though the data redundancy in general hampers the z coverage speed, some redundancy in this case helps to reduce artifacts.

The 6:1 helical pitch is provided for those applications demanding high volume coverage speed and thin slice scan, which are currently done with high (around 2:1) pitch single slice helical CT. It can be proven using the z sampling analysis that there are four helical pitches (i.e., pitch 2,4,6 and 8) of the 4-slice helical CT that can match the z sampling gap of the 2:1 pitch single slice helical CT, which is $d(=(p/2)d)$ with 180° LI. Although the consideration on the z coverage speed favors the high pitch (preferably, 8:1 pitch), the studies on image artifacts (such as the one shown in Fig. 7) indicate that there are more artifacts near the edge of the 8:1 pitch images (the 5th column) than the 6:1 pitch images (the 4th column). For this reason, the 6:1 pitch is chosen as a preferred tradeoff of the z-coverage speed and image artifacts for this class of applications.

Besides 3:1 and 6:1, other helical pitches (such as 8:1) can be provided in the future for different tradeoffs of the z coverage speed and various aspects of IQ to suit for different application requirements.

The 4-slice CT scanner discussed in this paper consists of a scalable 4-slice detector. To be specific, there are 16 detector cells with 1.25 mm cell size when measured along the z-axis. The detector row collimation can vary from 1.25, 2.5, 3.75, and 5 mm by selecting electronic switches to combine up to 4 individual detector cells in the z direction. With these four detector row collimation settings, the two preferred helical pitches (3:1 and 6:1) translate into eight scan modes, which provide six table translating distances per rotation. They are 3.75, 7.5, 11.25, 15, 22.5, and 30 mm/rot.

3. Assessment of the volume coverage speed performance of the 4-slice CT

It is noted from Fig. 5 and Table I that helical pitches 3 and 6 of the 4-slice CT have similar slice profiles to helical pitches 1 and 2, respectively, of the single slice CT. It is also noted from Table I that the increase of image noise from step-and-shoot to helical CT is less in the 4-slice CT with pitches 3:1 and 6:1 (5%) than in the single slice CT (15%). The reduction is due to the overlap of the beams defined by 1st and 4th detector rows when either 360° or 180° periodicity is considered.

We assess IQ (in terms of image artifacts and slice thickness) and the volume coverage speed performance of the 3:1 pitch 4-slice CT relative to the 1:1 pitch single slice CT by comparing two pairs of the images in the 2nd column of Fig. 7. The 2.5 mm image comparison (the 1st versus 3rd row) shows that the 3:1 pitch 4-slice CT can be 3 times as fast as the 1:1 pitch single slice CT, with equivalent or slightly more image artifacts. On the other hand, the 3.75 mm image comparison (the 2nd vs 4th row) indicates that the 3:1 pitch 4-slice CT can run twice as fast as the 1:1 pitch single slice CT, with less image artifacts.

Similar assessment can be made by comparing the 6:1 pitch 4-slice CT with the 2:1 pitch single slice CT (the 4th column in Fig. 7). The 3.18 mm image comparison (the 1st vs 3rd row) shows that the 6:1 pitch 4-slice CT can be 3 times as fast as the 2:1 pitch single slice CT, with more image artifacts. On the other hand, the 4.76 mm image comparison (the 2nd vs 4th row) indicates that the 6:1 pitch 4-slice CT can run twice as fast as the 2:1 pitch single slice CT with less image artifacts (i.e., image distortions).

These studies confirmed the z sample analysis (in the previous section), proving that 3:1 and 6:1 pitch 4-slice CT can provide equivalent IQ of 1:1 and 2:1 pitch single slice CT, respectively. Furthermore, they demonstrate that the 4-slice helical CT can provide equivalent IQ at 2 to 3 times the volume coverage speed of the single slice helical CT.

4. Other discussions

In this paper, we used an intuitive picture of interlacing helices to illustrate the concept of z-sampling efficiency and to predict image quality. This is an approximate analysis because, as shown in Fig. 4 and by Eq. (A3), a complementary fan-beam projection contains measurements at different z locations and the dashed helices in Figs. 2 and 3 represent the z locations of the center detector channel. Although these variations can be accounted for by a more rigorous analysis, involving the data sampling diagram such as Fig. 4 and equations such as (A3), the study shown in Secs. V B and V C indicates that this intuitive analysis serves the purpose of this study quite well.

With reference to Figs. 2(b) and 3(b) and the discussion in Secs. III B and V C 2, it is further noted that there are two requirements for achieving the z sampling gap of $d/2$ in multi-slice CT: first, the helical pitch is an odd integer so that the dashed helices bisect the gaps of the solid helices [refer to Fig. 3(b)]; second, the helical pitch is less than the number of detector rows so that there is no seam in x-ray beam coverage after each rotation. These two requirements combined lead to the conclusion that the 3:1 pitch is the highest helical pitch for the 4-slice CT that can match the z sampling gap of $d/2$.

To be specific, for 5:1 and 7:1 helical pitches of the 4-slice CT, the dashed helices cannot bisect the every gaps of the solid helices because of the seam of x-ray beam coverage after each rotation. [The case of helical pitch around 5:1 is shown in Fig. 2(b).] Thus, helical pitches of 5:1 and 7:1 result in an uneven sampling pattern, d for certain angular region and $d/2$ for the rest. Consequently, the image appearance is relatively unstable, depending on whether the challenging structure is sampled with $d/2$ or d spacing, which is determined by a clinically uncontrollable parameter β_0—the gantry rotation angle when the slice to be reconstructed passes the CT gantry plane. Given the complicated charac-

teristics of 5:1 and 7:1 helical pitches and the scope of this paper, we did not include the 5:1 and 7:1 helical pitches in Table I and Fig. 7. This would not affect any discussion and conclusion in this paper. Furthermore, it is noted that the IQ and the volume coverage speed performance of the 1:1 pitch 4-slice CT are similar to a 1:1 pitch single slice CT. To highlight the key results, the images of the 1:1 pitch 4-slice CT are not included in Fig. 7.

Most discussions in this paper, unless specified otherwise, apply to multi-slice helical CT in general. The general discussions include the concept of the preferred helical pitches, the general interpolation algorithm, and *z*-filtering reconstruction [Eqs. (4), (B2)–(B4)], and the theoretical models of slice profile and noise. Furthermore, all the discussions in this paper, although directly for fan-beam CT geometry, can be readily extended to the parallel-beam projections either collected directly or derived from fan beam projections. In particular, the algorithms work with the quarter-detector-offset CT system alignment.

VI. CONCLUSIONS

The scan and reconstruction principles of multi-slice helical CT have been presented. They include the preferred helical pitch; the helical interpolation algorithms; and the *z*-filtering reconstruction. The concept of the preferred helical pitch has been discussed in general with a newly proposed *z* sampling analysis. The helical interpolation algorithms and the *z*-filtering reconstructions have been developed for multi-slice CT. The theoretical models of slice profile and noise have been established for multi-slice helical CT. For the 4-slice helical CT in particular, preferred helical pitches have been selected. Special helical interpolation algorithms have been developed. Image quality of the 4-slice helical CT have been studied and compared with single slice helical CT. The results show that the slice profile, image artifacts, and noise exhibit performance peaks or valleys at certain helical pitches in multi-slice CT, whereas in single-slice CT the image noise remains unchanged and the slice profile and image artifacts steadily deteriorate with increasing helical pitch. The study indicates that the 4-slice helical CT can provide equivalent image quality at 2 to 3 times the volume coverage speed of the single slice helical CT.

ACKNOWLEDGMENTS

The author would like to thank Richard Kinsinger, Norbert Pelc, Armin Pfoh, Carl Crawford, Stan Fox, Sholom Ackelsberg, Bob Senzig, Gray Strong, H. David He, George Seidenschnur, and Tinsu Pan for their help at different stages of this research. The author wishes to express his sincere appreciation for the valuable comments and suggestions made by the anonymous associate editor and reviewers.

APPENDIX A: SPECIAL LI ALGORITHMS FOR THE 4-SLICE HELICAL CT

In this Appendix, we present special linear interpolation reconstruction algorithms for the 4-slice helical CT at pitches around 3:1[16] and 6:1,[17] respectively. The four rows of projection data are illustrated in Fig. 4 in the form of detector fan angle (the horizontal axis) versus the gantry rotation angle (the vertical axis). With reference to Fig. 4 and without loss of generality, it is assumed that the gantry rotation angle equals to 0 when the slice to be reconstructed passes the CT gantry plane [i.e., β_0 in Eq. (3a) equals to 0]. We use β_n to denote the gantry rotation angle when the reconstructed slice passes the fan beam defined by the nth detector row. It follows from Eqs. (3) that

$$\beta_n = 2Z_n\pi/p, \tag{A1}$$

where

$$Z_{[1-4]} = [-1.5, -0.5, 0.5, 1.5]. \tag{A2}$$

The parameter p is the helical pitch. The fan-beam projection of view β_n are shown as the solid lines in Fig. 4. Because of the z displacement of the multi-slice detector, β_n are shifted from one detector row to the next in the direction of the gantry rotation angle. Furthermore, we use $\beta_{n\pm}$ to denote the complementary data derived from the fan-beam projection of view β_n using the 180° periodicity. It then follows that

$$\beta_{n\pm} = \beta_n \pm \pi - 2\gamma = 2Z_n\pi/p \pm \pi - 2\gamma. \tag{A3}$$

The relative relationship of β_n and $\beta_{n\pm}$ is shown in Fig. 4 for helical pitch around 3:1. We use $W_n(\beta,\gamma)$ to denote the helical interpolation weighting function—the amount of contribution. From the special interlacing sampling pattern shown in Fig. 4, the helical interpolation weighting function is formulated as follows:

$$W_1(\beta,\gamma) = \alpha(x_1)\begin{cases} 0 & \beta \leqslant \beta_{2\_} \\ \dfrac{\beta-\beta_{2\_}}{\beta_1-\beta_{2\_}} & \beta_{2\_} < \beta \leqslant \beta_1 \\ \dfrac{\beta-\beta_{3\_}}{\beta_1-\beta_{3\_}} & \beta_1 < \beta < \beta_{3\_} \\ 0 & \beta \geqslant \beta_{3\_} \end{cases}, \tag{A4.1}$$

$$W_2(\beta,\gamma) = \begin{cases} 0 & \beta \leqslant \beta_{3\_} \\ \dfrac{\beta-\beta_{3\_}}{\beta_2-\beta_{3\_}} & \beta_{3\_} < \beta \leqslant \beta_2 \\ U_2(\beta,\gamma)+V_2(\beta,\gamma) & \beta_2 < \beta < \beta_M \\ 0 & \beta \geqslant \beta_M \end{cases}, \tag{A4.2}$$

where

$$U_2(\beta,\gamma) = \alpha(x_2)\begin{cases} 0 & \beta \leqslant \beta_2 \\ \dfrac{\beta-\beta_{1_+}}{\beta_2-\beta_{1_+}} & \beta_2 < \beta < \beta_{1_+} \\ 0 & \beta \geqslant \beta_{1_+} \end{cases},$$

and

$$V_2(\beta,\gamma)=(1-\alpha(x_2))\begin{cases}0 & \beta\leqslant\beta_2\\ \dfrac{\beta-\beta_{4\_}}{\beta_2-\beta_{4\_}} & \beta_2<\beta<\beta_{4\_},\\ 0 & \beta\geqslant\beta_{4\_}\end{cases}$$

$$W_3(\beta,\gamma)=\begin{cases}0 & \beta\leqslant\beta_m\\ U_3(\beta,\gamma)+V_3(\beta,\gamma) & \beta_m<\beta\leqslant\beta_3\\ \dfrac{\beta-\beta_{2_+}}{\beta_3-\beta_{2_+}} & \beta_3<\beta<\beta_{2_+},\\ 0 & \beta\geqslant\beta_{2_+}\end{cases}\quad\text{(A4.3)}$$

where

$$U_3(\beta,\gamma)=\alpha(x_2)\begin{cases}0 & \beta\leqslant\beta_{1_+}\\ \dfrac{\beta-\beta_{1_+}}{\beta_3-\beta_{1_+}} & \beta_{1_+}<\beta<\beta_3,\\ 0 & \beta\geqslant\beta_3\end{cases}$$

and

$$V_3(\beta,\gamma)=(1-\alpha(x_2))\begin{cases}0 & \beta\leqslant\beta_{4\_}\\ \dfrac{\beta-\beta_{4\_}}{\beta_3-\beta_{4\_}} & \beta_{4\_}<\beta<\beta_3,\\ 0 & \beta\geqslant\beta_3\end{cases}$$

$$W_4(\beta,\gamma)=(1-\alpha(x_3))\begin{cases}0 & \beta\leqslant\beta_{2_+}\\ \dfrac{\beta-\beta_{2_+}}{\beta_4-\beta_{2_+}} & \beta_{2_+}<\beta\leqslant\beta_4\\ \dfrac{\beta-\beta_{3_+}}{\beta_4-\beta_{3_+}} & \beta_4<\beta<\beta_{3_+}\\ 0 & \beta\geqslant\beta_{3_+}\end{cases}.\quad\text{(A4.4)}$$

In Eqs. (A4.3) and (A4.2), $\beta_M=\max(\beta_{1_+},\beta_{4\_})$ and $\beta_m=\min(\beta_{1_+},\beta_{4\_})$. It is noted that because of the redundancy between the measurements by the 1st and 4th detector rows, their contributions can be combined. The way of combination is controlled by $\alpha(x)$. $\alpha(x)=1/2$ if they are equally weighted.

The portions of data which have nonzero contribution to the reconstructed slice can be derived from Eqs. (A4). They are shown by the shaded regions of Fig. 4. This information is utilized to achieve fast (pipeline) data processing.

It can be proven that this algorithm is applicable in the following pitch range: $2\pi/(\pi-2\gamma_m)<$helical pitch $<4\pi/(\pi+2\gamma_m)$, where the $2\gamma_m$ denotes the fan angle. Given that $2\gamma_m\approx\pi/4$ on the scanner being discussed, this algorithm can be used for a helical pitch range of 2.6 $<$helical pitch$<$3.2.

Similarly, a linear interpolation algorithm for the 6:1 pitch 4-slice CT can be formulated as follows:

$$W_1(\beta,\gamma)=\frac{1}{2}\begin{cases}0 & \beta\leqslant\beta_{3\_}\\ \dfrac{\beta-\beta_{3\_}}{\beta_1-\beta_{3\_}} & \beta_{3\_}<\beta\leqslant\beta_1\\ \dfrac{\beta-\beta_2}{\beta_1-\beta_2} & \beta_1<\beta<\beta_2\\ 0 & \beta\geqslant\beta_2\end{cases},\quad\text{(A5.1)}$$

$$W_2(\beta,\gamma)=\begin{cases}0 & \beta\leqslant\beta_m\\ U_2(\beta,\gamma)+V_2(\beta,\gamma) & \beta_m<\beta\leqslant\beta_2\\ \dfrac{\beta-\beta_3}{\beta_2-\beta_3} & \beta_2<\beta<\beta_3,\\ 0 & \beta\geqslant\beta_3\end{cases}\quad\text{(A5.2)}$$

where

$$U_2(\beta,\gamma)=\frac{1}{2}\begin{cases}0 & \beta\leqslant\beta_1\\ \dfrac{\beta-\beta_1}{\beta_2-\beta_1} & \beta_1<\beta<\beta_2,\\ 0 & \beta\geqslant\beta_2\end{cases}$$

and

$$V_2(\beta,\gamma)=\frac{1}{2}\begin{cases}0 & \beta\leqslant\beta_{4\_}\\ \dfrac{\beta-\beta_{4\_}}{\beta_2-\beta_{4\_}} & \beta_{4\_}<\beta<\beta_2,\\ 0 & \beta\geqslant\beta_2\end{cases}$$

$$W_3(\beta,\gamma)=\begin{cases}0 & \beta\leqslant\beta_2\\ \dfrac{\beta-\beta_2}{\beta_3-\beta_2} & \beta_2<\beta\leqslant\beta_3\\ U_3(\beta,\gamma)+V_3(\beta,\gamma) & \beta_3<\beta<\beta_M\\ 0 & \beta\geqslant\beta_M\end{cases},\quad\text{(A5.3)}$$

where

$$U_3(\beta,\gamma)=\frac{1}{2}\begin{cases}0 & \beta\leqslant\beta_3\\ \dfrac{\beta-\beta_{1_+}}{\beta_3-\beta_{1_+}} & \beta_3<\beta<\beta_{1_+},\\ 0 & \beta\geqslant\beta_{1_+}\end{cases}$$

and

$$V_3(\beta,\gamma)=\frac{1}{2}\begin{cases}0 & \beta\leqslant\beta_3\\ \dfrac{\beta-\beta_4}{\beta_3-\beta_4} & \beta_3<\beta<\beta_4,\\ 0 & \beta\geqslant\beta_4\end{cases}$$

$$W_4(\beta,\gamma)=\frac{1}{2}\begin{cases}0 & \beta\leqslant\beta_3\\ \dfrac{\beta-\beta_3}{\beta_4-\beta_3} & \beta_3<\beta\leqslant\beta_4\\ \dfrac{\beta-\beta_{2_+}}{\beta_4-\beta_{2_+}} & \beta_4<\beta<\beta_{2_+}\\ 0 & \beta\geqslant\beta_{2_+}\end{cases}. \quad \text{(A5.4)}$$

In Eqs. (A5.2) and (A5.3), $\beta_m=\min(\beta_1,\beta_{4\_})$, and $\beta_M=\max(\beta_4,\beta_{1+})$. The pitch range of this algorithm can be formulated as $4\pi/(\pi-2\gamma_m)<\text{helical pitch}<6\pi/(\pi-2\gamma_m)$. Given that $2\gamma_m\approx\pi/4$, this algorithm can be used for a helical pitch range of $5.3<\text{helical pitch}<8$.

APPENDIX B: *Z*-FILTERING RECONSTRUCTION ALGORITHMS

The mathematical framework for reconstructing a composite slice with different thickness can be described as follows:[19] we denote a set of reconstructed slices as $I(x,y,z)$, where z represents a set of the image locations along the z axis. A new set of the composite slices, denoted as $\tilde{I}(x,y,z)$, can conceptually be derived from the original reconstructions $I(x,y,z)$ by the following convolution:

$$\tilde{I}(x,y,z)=\int h(z')I(x,y,z-z')dz', \quad \text{(B1)}$$

where $h(\,)$ is the z filtering kernel along the z axis. Thus, the composite slice, $\tilde{I}(x,y,z)$, is a weighted average of the original reconstruction, $I(x,y,z)$.

The composite slice can also be reconstructed directly without generating any original slice. For the helical CT, we use $W_n(\beta,\gamma)$ and $\tilde{W}_n(\beta,\gamma)$ to denote the helical interpolation weighting functions employed in the original reconstruction and the z-filtering reconstruction, respectively. From Eq. (B1) and the linearity property of the reconstruction, the helical weighting function for the z-filtering reconstruction, $\tilde{W}_n(\beta,\gamma)$, can be formulated as a convolution of the same z-filtering kernel, $h(\,)$, with the original helical weighting function, $W_n(\beta,\gamma)$, as follows:

$$\tilde{W}_n(\beta,\gamma)=\int h(\beta')W_n(\beta-\beta',\gamma)d\beta', \quad \text{(B2)}$$

where, β' characterizes the amount of shift in the rotational direction that corresponds, according to Eq. (3), to the z-shift z' in Eq. (B1).

Equation (B2) can be written in the discrete form as follows:

$$\tilde{W}_n(\beta,\gamma)=\sum_{i=-m}^{m}h(i)W_n(\beta-i\Delta\beta,\gamma), \quad \text{(B3)}$$

where $h(i)$ is a discrete kernel of the length of $2m+1$; the $\Delta\beta$ is the kernel spacing, or the amount of β-shift in $W_n(\beta,\gamma)$ from one term to the next. The z-filtering parameters [i.e., $\Delta\beta$, m and $h(i)$] in Eq. (B3) control the slice-thickness, image noise, and artifacts.

As an alternative approach,[16] the z-filtering reconstruction can directly be integrated into the helical interpolation algorithm as follows using the nomenclatures defined in Sec. IV A. To derive a fan-beam projection measurement $P(\beta,\gamma)$ at the slice location z_0, all the measurements along the path of (β,γ), denoted as $P^i(\beta,\gamma)$, can be used, where i is an index that runs over all the measurements at (β,γ), including both original and complementary data and regardless of which detector row produces it. The z location of each measurement is denoted as z_i, which can be computed from Eqs. (3) given the (β,γ) and the detector row index n. Thus, a new linear combination method can be formulated in general as follows:

$$\beta,\gamma)=\sum_i\left[w(z_i-z_0)P^i(\beta,\gamma)\right]\Big/\sum_i w(z_i-z_0). \quad \text{(B4)}$$

The width of $w(z)$ controls the slice thickness, image noise, and artifacts. One possible shape for $w(z)$ is a triangle with amplitude of 1 at $z_i=z_0$ and value of 0 at $z_i=z_0\pm\Delta z$.

[a]Present affiliation and address: Imaging Tech, Inc., 20720 W. Watertown Rd., Suite 201, Waukesha, WI 53186.
[b]Present electronic-mail: hui.hu@imagingtechinc.com

[1]I. Mori, ''Computerized tomographic apparatus utilizing a radiation source,'' U.S. Patent No. 4 630 202, 1986.
[2]H. Nishimura and O. Miyazaki, ''CT system for spirally scanning subject on a movable bed synchronized to x-ray tube revolution,'' U.S. Patent No. 4 789 929, 1988.
[3]C. R. Crawford and K. F. King, ''Computed tomography scanning with simultaneous patient translation,'' Med. Phys. **17**, 967–982 (1990).
[4]W. A. Kalender, W. Seissler, E. Klotz *et al.*, ''Spiral volumetric CT with single-breath-hold technique, continuous transport, and continuous scanner rotation,'' Radiology **176**, 181–183 (1990).
[5]A. Polacin, W. A. Kalender, and G. Marchal, ''Evaluation of section sensitivity profiles and image noise in spiral CT,'' Radiology **185**, 29–35 (1992).
[6]J. Hsieh, ''A general approach to the reconstruction of x-ray helical computed tomography,'' Med. Phys. **23**, 221–229 (1996).
[7]J. A. Brink, J. P. Heiken, D. M. Balfe *et al.*, ''Spiral CT: Decreased spatial resolution *in vivo* due to broadening of section-sensitivity profile,'' Radiology **185**, 469–474 (1992).
[8]J. A. Brink, J. P. Heiken, G. Wang *et al.*, ''Helical CT: Principles and technical considerations,'' Radiographics **14**, 887–893 (1994).
[9]J. S. Arenson, R. Levinson, and D. Freundlich, ''Dual slice scanner,'' U.S. Patent No. 5 228 069, 1993.
[10]Y. Liang and R. A. Kruger, ''Dual-slice spiral versus single-slice spiral scanning: Comparison of the physical performance of two computed tomography scanners,'' Med. Phys. **23**, 205–220 (1996).
[11]L. Feldkamp, L. Davis, and J. Kress, ''Practical cone-beam algorithm,'' J. Opt. Soc. Am. 612–619 (1984).
[12]H. Hu, ''An improved cone-beam reconstruction algorithm for the circular orbit,'' Scanning **18**, 572–581 (1996).
[13]H. Kudo and T. Stato, ''Helical-scan computed tomography using cone-beam projections,'' in IEEE NSS/MIC (1991).
[14]G. Wang, T.-H. Lin, and P. C. Cheng, ''A general cone-beam reconstruction algorithm,'' IEEE Trans. Med. Imaging **12**, 486–496 (1993).
[15]S. Schaller, T. Flohr, and P. Steffen, ''A new, efficient Fourier-reconstruction method for approximate image reconstruction in spiral cone-beam CT at small cone-angles.,'' in SPIE International Symposium on Medical Imaging, 1997.

[16]H. Hu and N. Pelc, ''Systems, methods, and apparatus for reconstructing images in a CT system implementing a helical scan,'' U.S. Patent No. 5 559 847, 1996.
[17]H. Hu, ''Image reconstruction for a CT system implementing a four fan beam helical scan,'' U.S. Patent No. 5 541 970, 1996.
[18]H. Hu and Y. Shen, ''Helical CT reconstruction with longitudinal filtration,'' Med. Phys. **25**, 2130 (1998).
[19]H. Hu, ''Method and apparatus for multislice helical image reconstruction in a computer tomography system,'' U.S. Patent No. 5 606 585, 1997.
[20]H. Hu and Y. Shen, ''Helical reconstruction algorithm with user-selectable section profile,'' in RSNA, 189 (1996).
[21]W. A. Kalender and A. Polacin, ''Physical performance characteristics of spiral CT scanning,'' Med. Phys. **18**, 910–915 (1991).
[22]G. Wang and M. W. Vannier, ''Helical CT image noise: Analytical results,'' Med. Phys. **20**, 1635–1640 (1993).
[23]G. Wang and M. W. Vannier, ''Longitudinal resolution in volumetric x-ray computerized tomography: Analytical comparison between conventional and helical computerized tomography,'' Med. Phys. **21**, 429–433 (1994).
[24]H. Hu and S. H. Fox, ''The effect of helical pitch and beam collimation on the lesion contrast and slice profile in helical CT imaging,'' Med. Phys. **23**, 1943–1954 (1996).